Available online at www.sciencedirect.com
ScienceDirect
Trans. Nonferrous Met. Soc. China 34(2024) 952−965
Transactions of Nonferrous Metals Society of China
www.tnmsc.cn

First-principles investigation on structural, thermodynamic, and elastic properties of suboxide Zr_3O phase

Hong-ling ZHOU[1], Li-jun CHEN[1], Xiao-ling YANG[1], Xu-yang LIU[2], Chao SUN[3], Bai-feng LUAN[1,4]

1. International Joint Laboratory for Light Alloys (Ministry of Education), Shenyang National Laboratory for Materials Science, College of Materials Science and Engineering, Chongqing University, Chongqing 400044, China;
2. College of Aerospace Engineering, Chongqing University, Chongqing 400044, China;
3. Science and Technology on Reactor Fuel and Materials Laboratory, Nuclear Power Institute of China, Chengdu 610213, China;
4. State Key Laboratory of Mechanical Transmissions, Chongqing University, Chongqing 400044, China

Received 7 June 2023; accepted 5 December 2023

Abstract: The lattice dynamics and finite-temperature thermodynamic and mechanical properties of three Zr_3O polymorphs, including rhombohedral ($R\bar{3}c$), rhombohedral ($R32$), and hexagonal ($P6_322$) phases, were theoretically investigated using the first-principles calculations. The calculated lattice parameters agree well with experimental values. It is confirmed that the three Zr_3O phases exhibit both dynamic and thermodynamic stability. The entropy, enthalpy, Gibbs free energy, specific heat capacity, thermal expansion coefficient, and elastic modulus as a function of temperature from 0 to 1500 K were systematically evaluated. It is found that Zr_3O ($R\bar{3}c$) is the ground state at 0 K followed by Zr_3O ($R32$) and Zr_3O ($P6_322$). Structural phase transitions occur from Zr_3O ($R\bar{3}c$) to Zr_3O ($R32$) at 50 K and then to Zr_3O ($P6_322$) at 540 K. Zr_3O ($R32$) displays superior mechanical properties compared to the other two Zr_3O phases.

Key words: first-principles; Zr_3O; lattice dynamics; thermodynamic properties; elastic modulus

1 Introduction

Zirconium (Zr) alloys have been used as nuclear fuel-rod cladding and structural components in light water reactors in water-cooled nuclear reactors since the 1950s due to their low thermal neutron absorption cross-section, excellent high-temperature corrosion resistance and good mechanical properties [1−3]. However, in a loss of coolant accident (LOCA), the violent reaction between high-temperature steam and Zr alloy can release a substantial amount of oxygen and heat. This leads to the rapid oxidation of Zr alloys in the high-temperature and high-humidity service environment, significantly limiting their practical applications [4,5]. Therefore, identifying the oxidation mechanisms and improving the oxidation/corrosion properties are crucial in their industrial application.

To this end, significant efforts have been devoted to the experimental investigations of the oxidation/corrosion of Zr alloys in the past decades [3−8]. Besides ZrO_2, other stoichiometries of zirconium suboxides, such as ZrO, Zr_3O and Zr_6O, have also been identified at the zirconium/zirconium oxide interface during the oxidation of Zr alloys. Notably, many scholars have carried out

Corresponding author: Chao SUN, Tel: +86-28-85900598, E-mail: sunchaonpic@qq.com;
Bai-feng LUAN, Tel:+86-23-65106067, E-mail: bfluan@cqu.edu.cn
DOI: 10.1016/S1003-6326(23)66445-3

comprehensive research on ZrO_2 [9−11], and these suboxides have received great attention [12]. Theoretical calculations indicated that the ground state structure of ZrO was $P\bar{6}2m$ and stable up to 1300 K or 1500 K [8,13,14]. At the same time, Zr_6O suboxide was detected in thin foils of oxidized zirconium by selected area diffraction [15], and then ARAI and HIRABAYASHI [16] reported the structure of Zr_6O to be isomorphic with $P\bar{3}1c$-Ti_6O and $P\bar{3}1c$-Hf_6O. $R\bar{3}$-Zr_6O was proved to be the ground state structure using the first principles calculation [13]. For Zr_3O, ILTIS and MICHEL [17] and YILMAZBAYHAN et al [18] have identified the existence of this ordered phase in a narrow spatial domain near the oxide/metal interface of Zr-4 alloy by electron microdiffraction. CHOUDHURI et al [5] also observed the presence of suboxide Zr_3O in the oxide layer near the oxide−coolant interface in the irradiated in-pile Zr-4 fuel tube material. Unfortunately, although different experimental [5,19−21] and computational [13,14,22−26] approaches have been used to investigate the appearance of suboxide Zr_3O, the determination of its crystal structure is still under debate. The calculated results using the first principles suggested that the experimental suboxide Zr_3O belongs to the rhombohedral structure ($R\bar{3}c$) [14]. However, CHOUDHURI et al [5] found that Zr_3O ($R32$) with the rhombohedral system was formed in the oxide layer of Zr-4 alloy as the pressurized heavy water reactor (PHWR) fuel tube material during its residence in the reactor. HOLMBERG and DAGERHAMN [24] also reported that the structure of Zr_3O was isostructural with the Ni_3N type (Space group $P6_322$) by employing the X-ray diffraction method, and then this Zr_3O structure formed in Zr-based alloy was confirmed using the neutron diffraction studies by YAMAGUCHI [25] and RIABOV et al [26].

Hence, despite being a commonly observed suboxide during Zr-based alloy oxidation, the crystal structure of its most stable phase and corresponding thermodynamic and mechanical properties at finite temperatures of the Zr_3O phases have not been well understood. These properties are of utmost importance for comprehending the oxidation/corrosion behavior of Zr-based alloy for industrial and engineering applications. Unfortunately, measuring these properties under extreme conditions, such as high temperatures, poses a significant challenge. As a result, this study aims to thoroughly investigate the structural stability, lattice dynamics, and finite-temperature thermodynamic and elastic properties of Zr_3O phases by applying systematic first-principles calculations. The calculated results for Zr_3O are consistent with experimental measurements and/or existing calculations. The predicted structural, thermodynamic, and elastic properties of the three different structures of Zr_3O in this study could provide a guideline for the experimental research of Zr_3O.

2 Crystal structures and calculation details

2.1 Crystal structure

Figure 1 shows the selected three different crystal structures of Zr_3O, i.e., rhombohedral Zr_3O (Space group $R\bar{3}c$), rhombohedral Zr_3O (Space group $R32$), and hexagonal Zr_3O (Space group $P6_322$). The structure of Zr_3O ($R\bar{3}c$) obtained from Ref. [27] contains six units of Zr_3O and is shown in Fig. 1(a). The experimental lattice parameters of the suboxide Zr_3O ($R\bar{3}c$) are a=b=5.650 Å, c=15.643 Å, α=β=90°, and γ=120°. Zr atoms only occupy the rhombohedral sites in Zr_3O, and the O atoms stack closely in ABCABC style. The model of Zr_3O (Fig. 1(b)) is adopted from Ref. [28]. It is reported to possess a rhombohedral symmetry with the space group $R32$. The experimental lattice parameters of the rhombohedral Zr_3O ($R32$) oxide are a=b= 5.645 Å, c=31.293 Å, α=β=90°, and γ=120°. The crystal structure of the Zr_3O (Fig. 1(c)) unit cell belongs to the hexagonal symmetry with space

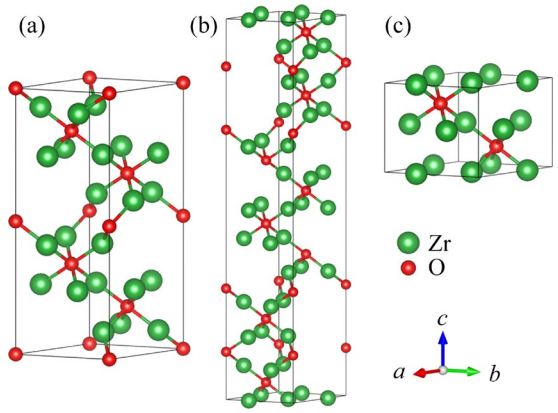

Fig. 1 Projections of crystal structures of Zr_3O (Space group $R\bar{3}c$) (a) [27], Zr_3O (Space group $R32$) (b) [28], and Zr_3O (Space group $P6_322$) (c) [24]

group $P6_322$, containing two formula units per cell. The experimental lattice parameters of the hexagonal Zr_3O ($P6_322$) are $a=b$=5.642 Å, c=5.224 Å, $\alpha=\beta$=90°, and γ=120° [24].

2.2 Calculation details

Firstly, we calculate the Helmholtz free energy (F) by the following equation [29−31] to determine the relative phase stability of the three different structures of Zr_3O:

$$F(T,V)=E_{\text{static}}(V)+F_{\text{vib}}(T,V)+F_{\text{elec}}(T,V) \quad (1)$$

where E_{static} represents the static energy, F_{vib} is the lattice vibrational free energy, F_{elec} refers to the thermal electron free energy induced by the thermal electronic excitation, and T and V are temperature and volume, respectively. Based on phonon theory, F_{vib} can be expressed as [32]

$$F_{\text{vib}}(T,V)=k_{\text{B}}T\int \ln[2\sinh(\frac{\hbar\omega}{2k_{\text{B}}T})]\,g(\omega,V)\mathrm{d}\omega \quad (2)$$

where k_{B} is the Boltzmann constant, $\hbar$ refers to the reduced Planck's constant, and $g(\omega,V)$ represents the phonon density-of-states (PDOS) with ω being the phonon frequency. The vibrational entropy (S_{vib}) and specific heat capacity (C_{vib}) are calculated by

$$S_{\text{vib}}(T,V)=k_{\text{B}}\int_0^{\infty}\left\{\frac{[\hbar\omega/(k_{\text{B}}T)]}{\exp[\hbar\omega/(k_{\text{B}}T)]-1}-\ln\left[1-\exp(-\hbar\omega/(k_{\text{B}}T))\right]\right\}g(\omega,V)\mathrm{d}\omega \quad (3)$$

$$C_{\text{vib}}(T,V)=k_{\text{B}}\int_0^{\infty}\frac{[\hbar\omega/(k_{\text{B}}T)]^2\exp[\hbar\omega/(k_{\text{B}}T)]}{\left[\exp(\hbar\omega/(k_{\text{B}}T))-1\right]^2}\cdot g(\omega,V)\mathrm{d}\omega \quad (4)$$

The Helmholtz free energies are calculated at seven fixed volumes around the equilibrium volume with a volume interval of 4.5% to facilitate the quasiharmonic approach. Then, the results are fitted using the modified Birch−Murnaghan equation of states [33]

$$F(T,V)=a+bV^{-2/3}+cV^{-4/3}+dV^{-2} \quad (5)$$

where a, b, c, and d are fitting parameters.

Thus, the equilibrium volume V_{eq} at zero pressure and given temperature can be obtained by the following equation:

$$-\left(\frac{\partial F(T,V)}{\partial V}\right)_T=0 \quad (6)$$

Then, the thermodynamic properties, including thermal expansion coefficient (α), specific heat capacity at constant pressure (C_p), and bulk modulus (B) are calculated by the following equations:

$$\alpha(T)=\frac{1}{3V_{\text{eq}}(T)}\left(\frac{\partial V_{\text{eq}}(T)}{\partial T}\right)_p \quad (7)$$

$$C_p=C_{\text{vib}}+\beta^2BTV \quad (8)$$

$$B(T,V)=V\left(\frac{\partial^2F(V,T)}{\partial V^2}\right)_T \quad (9)$$

where $\beta=3\alpha$.

The Debye temperature (Θ_{D}) is calculated by fitting the calculated C_{vib} in Eq. (4) using the following equation:

$$C_{\text{vib,Debye}}(T)=9k_{\text{B}}\left(\frac{T}{\Theta_{\text{D}}(T)}\right)^3\int_0^{\Theta_{\text{D}}(T)/T}\frac{x^4\mathrm{e}^x}{(\mathrm{e}^x-1)^2}\mathrm{d}x \quad (10)$$

where $x=\hbar\omega/(k_{\text{B}}T)$.

Finally, the temperature dependences of the elastic stiffness coefficients and elastic properties are calculated according to Refs. [34,35].

In this work, we used the Vienna ab initio simulation package (VASP) to perform the first-principles calculations [36]. The ion-electron interaction is described by using the full potential frozen core projector augmented wave (PAW) method. The exchange–correction functionals are adopted by the generalized gradient approximation (GGA), local density approximation (LDA), and Perdew, Burke and Ernzerhof (PBE) implementation of the generalized gradient approximation. The cutoff energy of the Zr_3O is 520 eV.

In the crystal structure relaxation calculation, ISIF=3 was performed to allow the volume, ionic positions, and shape of the cells to vary; the Γ-centered k-points are set as 5×5×2 for Zr_3O ($R\bar{3}c$), 6×6×1 for Zr_3O ($R32$), and 6×6×5 for Zr_3O ($P6_322$), respectively. The geometry optimizations are performed using the conjugate gradient algorithm until the forces acting on the ions are less than 1×10^{-3} eV/Å. The total energy change was converted to be 1×10^{-8} eV per cell. Then, the Γ-centered k-points are set as 8×8×3 for Zr_3O ($R\bar{3}c$), 7×7×2 for Zr_3O ($R32$), and 8×8×7 for Zr_3O ($P6_322$), respectively, to get the accurate static energies after

crystal relaxation. After that, we adopt the phonon calculations by using the YPHON package [37] to calculate the lattice dynamics and properties using the supercell method, with the 2×2×2 supercell for Zr_3O ($R\bar{3}c$) and Zr_3O ($R32$) and a 3×3×3 supercell for Zr_3O ($P6_322$), consisting of 192, 128, and 216 atoms, respectively. All the structures use the Γ-centered k-point of 3×3×3 in the phonon calculations. Finally, the Γ-centered k-points of 15×15×5 for Zr_3O ($R\bar{3}c$), 10×10×2 for Zr_3O ($R32$), and 15×15×14 for Zr_3O ($P6_322$), are carried out for the elastic properties calculation.

3 Results and discussion

3.1 Static energy

It is widely known that the choice of exchange-correlation function affects the optimized volume and energy in a DFT calculation. To verify the robustness of our results against the selection of the exchange-correlation function, we repeat the calculations using the LDA, the GGA, and the PBE to calculate the volume and static energy of the three Zr_3O structures. The calculated equilibrium volumes and static energies for the three Zr_3O structures at 0 K are collected in Table 1. Compared to the pseudopotentials of LDA and GGA, the calculated results using the PBE pseudopotential are much closer to the experimental results [24,27,28]. This indicates that the PBE gives a good account of thermodynamic and elastic properties for Zr_3O compared with the LDA and GGA. Therefore, we only employ the PBE pseudopotential in the following calculations.

Table 2 shows the calculated lattice constants for the three Zr_3O structures at 0 K, which agree well with the experimental results and reported calculation results [24,27,28]. The static energy−volume curves for the three different Zr_3O structures at 0 K are plotted in Fig. 2. The calculated equilibrium volumes and static energies (Table 1) also agree with the experimental results. The calculated equilibrium lattice parameters and equilibrium volumes of these phases are a little larger than those reported by BURTON et al [22], WEI et al [23], and HOHMBERG and DAGERHAMN [24], due to the usage of PBE (PBE typically underbids the system and thus tends to give relatively large cell volumes as compared to experiments [38]). Notably, the deviation of the computed equilibrium lattice parameters from experimental values is less than 0.33%, demonstrating the reliability of the current computational method. Among the three structures, the Zr_3O ($R\bar{3}c$) has the lowest static energy at its equilibrium volume, while the Zr_3O ($P6_322$) has the highest. However, it is found that the calculated static energy of all Zr_3O structures are negative, indicating that the three Zr_3O structures

Table 1 Predicted static properties for three Zr_3O structures, including equilibrium volume and total energy using different pseudopotentials

Phase	Space group	Method	Volume/ (Å^3·atom^{-1})	Energy/ (eV·atom^{-1})
Zr_3O	$R\bar{3}c$	Cal. (LDA)	17.045	−9.920
		Cal. (GGA)	18.195	−8.965
		Cal. (PBE)	18.068	−9.032
		Ref. [27]	18.022	−9.020
Zr_3O	$R32$	Cal. (LDA)	17.029	−9.920
		Cal. (GGA)	18.181	−8.964
		Cal. (PBE)	18.053	−9.031
		Ref. [28]	17.994	−9.020
Zr_3O	$P6_322$	Cal. (LDA)	17.015	−9.916
		Cal. (GGA)	18.175	−8.961
		Cal. (PBE)	18.040	−9.027
		Ref. [24]	17.998	−9.015

Table 2 Calculated and experimental structure parameters for three Zr_3O structures

Phase	Space group	Method	a/Å^3	b/Å^3	c/Å^3	α/(°)	β/(°)	γ/(°)
Zr_3O	$R\bar{3}c$	Calc.	5.659	5.659	15.635	90	90	120
		Ref. [27]	5.650	5.650	15.643	90	90	120
Zr_3O	$R32$	Calc.	5.655	5.655	31.279	90	90	120
		Ref. [28]	5.645	5.645	31.293	90	90	120
Zr_3O	$P6_322$	Calc.	5.652	5.652	5.216	90	90	120
		Ref. [24]	5.642	5.642	5.224	90	90	120

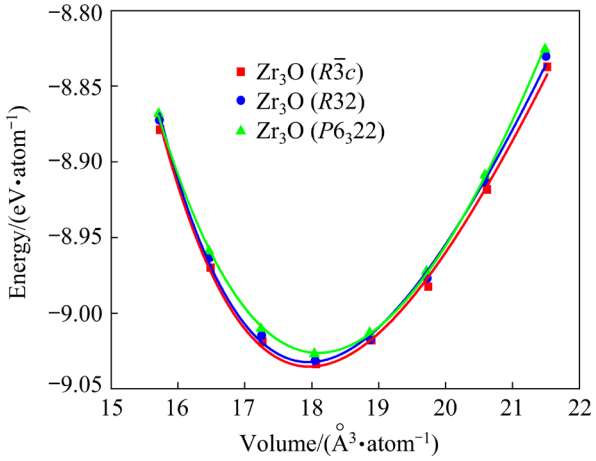

Fig. 2 Calculated static energies for three considered Zr_3O structures

are thermodynamically stable. Importantly, we also note that the calculated static energy of the three Zr_3O structures are very close, which implies that the external condition can easily result in the phase transition of Zr_3O.

Since Zr_3O ($R\bar{3}c$) and Zr_3O ($R32$) have the same rhombohedral structure, the features of these two structures are similar. According to Figs. 1(a) and (b), the structural stability of the rhombohedral Zr_3O ($R\bar{3}c$) and Zr_3O ($R32$) structure is related to the cohesive force of Zr—O—Zr sandwich layered structure along the c axis, which is reflected by the bond length of Zr—O. However, the structural feature of the hexagonal Zr_3O ($P6_322$) structure is much different from that of the two rhombohedral Zr_3O structures. The O atom of Zr_3O ($P6_322$) insets into the Zr icosahedral structure (Fig. 1(c)), indicating that the structural stability of the hexagonal Zr_3O ($P6_322$) also depends on the Zr—O bond. Therefore, we further calculated the bond length of Zr—O to explore the structural stability of the three Zr_3O structures. In this work, the estimated Zr—O bond length of Zr_3O ($R\bar{3}c$) is 2.275 Å, the shortest Zr—O bond length of Zr_3O ($R32$) is 2.280 Å and the longest Zr—O bond length is 2.290 Å. The calculated Zr—O bond length of Zr_3O ($P6_322$) is 2.278 Å, which is in good agreement with the value in Ref. [39]. Based on the analysis above, it can be concluded that the rhombohedral Zr_3O ($R\bar{3}c$) structure has better thermodynamic stability than the other two Zr_3O structures, which agrees well with the results reported by PAN [39].

3.2 Lattice dynamics

The phonon density-of-states further reflects the stability of a compound, and no negative frequency means the stability of the compound [40]. Figures 3(a), (c), and (e) show the partial phonon density-of-states (PDOS) due to the individual atoms for the three Zr_3O structures, respectively, which possess similar shapes. In addition, the total PDOS and the generalized phonon density-of-states (GPDOS) [41] of the three Zr_3O structures were calculated and shown in Figs. 3(b), (d), and (e). The total PDOS is the simple summation of contributions from Zr and O atoms. Notably, usually for oxides, PDOS cannot be measured directly through experiments. In this case, the measured data mainly refer to the neutron scattering cross-section weighted PDOS, namely GPDOS, which can be calculated by the following equation:

$$\mathrm{GPDOS}=\sum_i \frac{\sigma_i}{m_i}\mathrm{PDOS}_i \tag{11}$$

where σ_i and m_i mean the atomic scattering cross-section and the atomic mass for each element, respectively; PDOS_i refers to the projected partial PDOS for individual atoms.

It can be seen from Fig. 3 that no negative frequency is obtained in the three Zr_3O structures. Therefore, it is further demonstrated that the three Zr_3O structures are stable. The difference in the vibrational spectrum of these phases is better visible on the PDOS plots. These plots reveal that the three Zr_3O structures possess two distinct regions, dividing the spectrum into separate parts below and above 10 THz. In particular, the lattice vibration of the high-frequency region is related to the O atom, and the contributions of O in Zr_3O are limited to the region between 11 and 13 THz. However, the lattice vibration of the low-frequency region below 10 THz is attributed to the Zr atom due to the larger atomic mass.

Notably, the structural stability of the suboxide Zr_3O is related to the dynamical stability in addition to thermodynamic stability. Therefore, we further investigate the phonon dispersion of the three Zr_3O structures. For the phonon dynamically, no imaginary phonon frequency indicates the dynamical stability of a compound, and vice versa [42]. The calculated phonon dispersion spectra along some high symmetry directions for

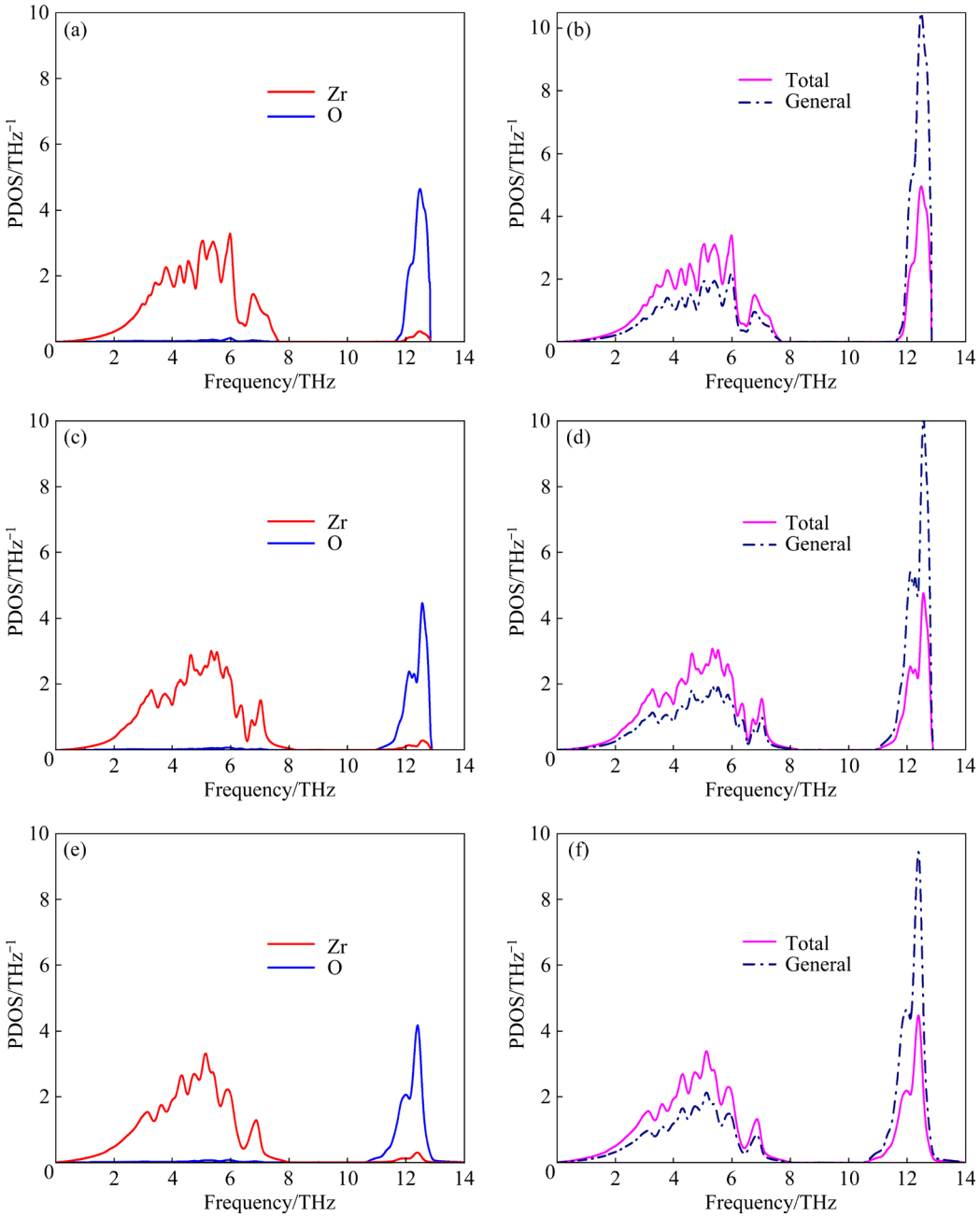

Fig. 3 Calculated partial, total and generalized phonon density-of-states (PDOS) for Zr_3O ($R\bar{3}c$) (a, b), Zr_3O ($R32$) (c, d), and Zr_3O ($P6_322$) (e, f) (The label "Total" refers to PDOS due to simple summation of contributions from Zr and O atoms and label "General" refers to neutron scattering cross-section weighted PDOS)

the three Zr_3O structures at their corresponding theoretical static equilibrium volumes at 0 K are presented in Fig. 4. The spectrum has a rather complicated structure, as Zr_3O ($R\bar{3}c$) has 72 different branches, Zr_3O ($R32$) has 48 different branches, and Zr_3O ($P6_322$) has 24 different modes. The phonon dispersion of Zr_3O is composed of high-frequency and low-frequency regions, which is demonstrated by the PDOS of the suboxide Zr_3O, as seen in Fig. 3. It can be observed that in the range of 2−7 THz and 12−14 THz, higher density phonon branches exist for the three Zr_3O structures. The critical feature is that the frequencies of Zr_3O ($R\bar{3}c$), Zr_3O ($R32$), and Zr_3O ($P6_322$) structures (Fig. 4) are positive. This indicates that these three structures are dynamically stable in a crystalline phase. The results of the lattice dynamics in this work are in good agreement with the reported results [39], further confirming the reliability of the current computational method.

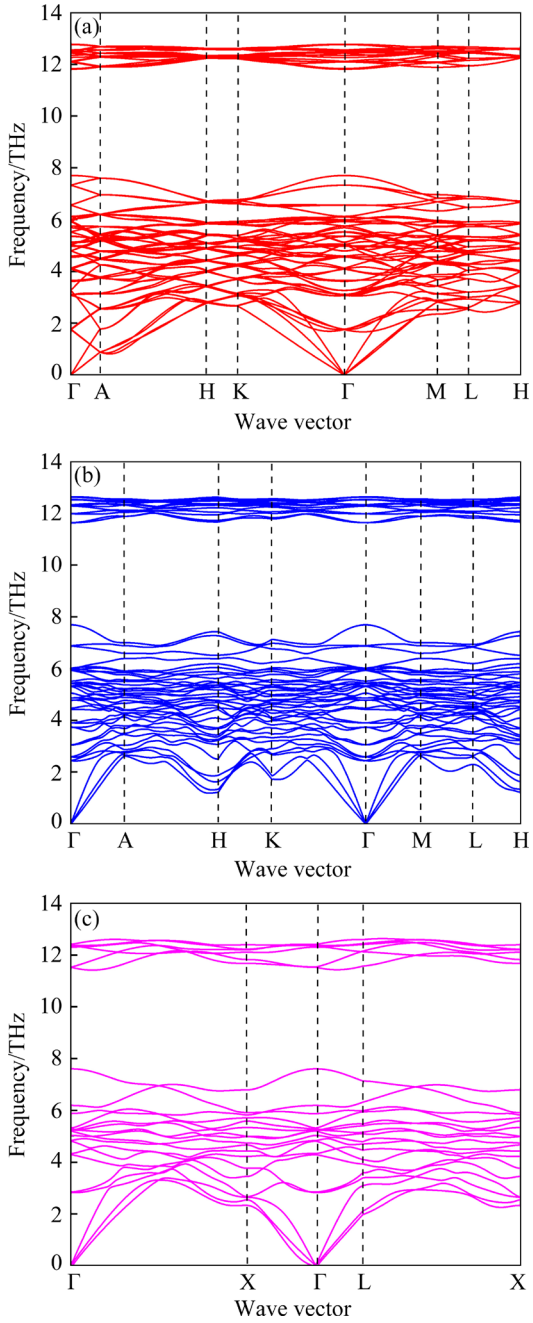

Fig. 4 Calculated phonon dispersion spectra of three Zr_3O structures: (a) Zr_3O ($R\bar{3}c$); (b) Zr_3O ($R32$); (c) Zr_3O ($P6_322$)

3.3 Temperature-dependent thermodynamic properties

This work also considered the temperature effect on the entropy, enthalpy, and total energies for the three Zr_3O structures. Figure 5 shows the variation of entropy, enthalpy, and Gibbs free energy with increasing the temperature from 0 to 1500 K for Zr_3O ($R\bar{3}c$), Zr_3O ($R32$), and Zr_3O ($P6_322$). It can be observed that the entropy and enthalpy of the three Zr_3O structures all increase with the rising temperature, and the entropy and enthalpy of the three Zr_3O structures show minimal differences. Especially, Zr_3O ($P6_322$) possesses the highest entropy while Zr_3O ($R\bar{3}c$) has the lowest, indicating the structure of Zr_3O ($R\bar{3}c$) has the most order while Zr_3O ($P6_322$) has the most chaos among the three Zr_3O structures.

Figure 5(c) shows the Gibbs free energies as a function of temperature at 0 GPa for the three phases. The Gibbs free energies continuously

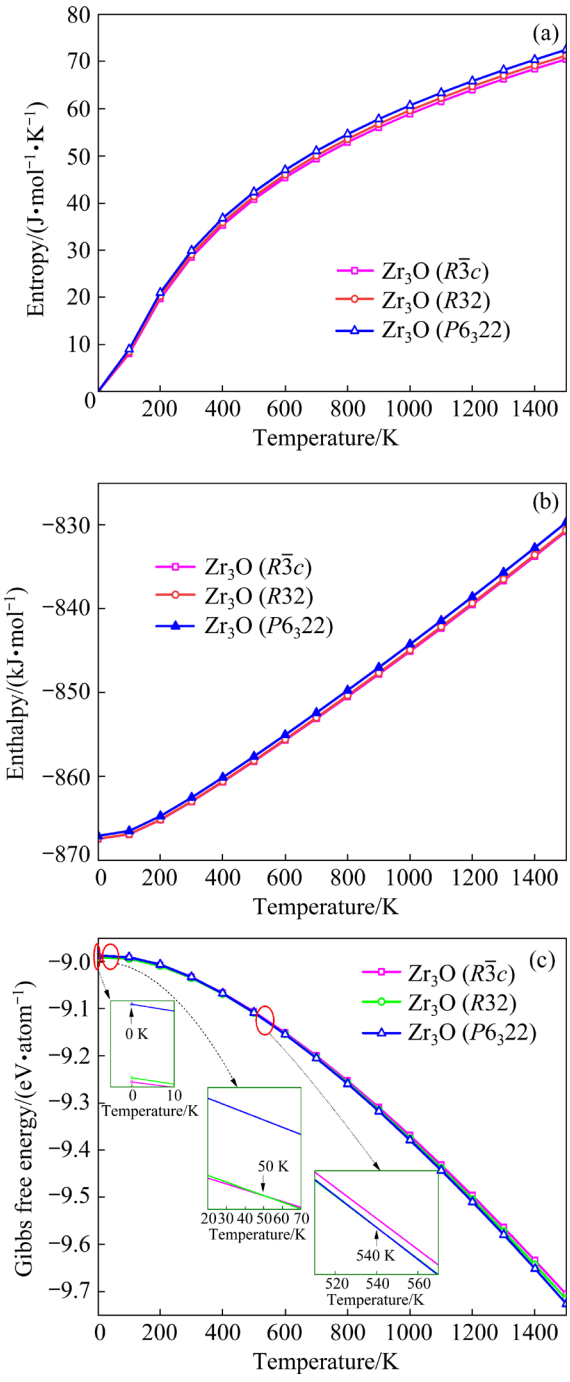

Fig. 5 Calculated entropy (a), enthalpy (b), and Gibbs free energy (c) as function of temperature for Zr_3O ($R\bar{3}c$), Zr_3O ($R32$), and Zr_3O ($P6_322$)

decrease with increasing the temperature from 0 to 1500 K. The Gibbs free energy of Zr_3O ($R\bar{3}c$) ranks the lowest among the three structures at 0 K. It is worth noting that with the increase of temperature from 50 to 540 K, the Gibbs free energy of Zr_3O ($R32$) turns out to be the lowest, while Zr_3O ($P6_322$) has the lowest Gibbs free energy when the temperature is above 540 K, indicating that the temperature rise could lead to the transition among the three structures. The experimental results also confirm this transition. FOORD and NEWCOMB [43] occasionally observed Zr_3O ($R\bar{3}c$) on Zr-4 alloy in pure oxygen at 500 °C and found that this structure was absent after transition. A similar phase transformation of Zr_3O was reported by ZHANG et al [14]. In their calculations, Zr_3O ($P6_322$) can be stable in the temperature range of 700−2000 K. These computational predictions were confirmed in our recent experimental study [44]. The phase with an approximate Zr_3O stoichiometry formed in Zr−1.0Nb−0.01Cu alloy that was oxidized isothermally in steam at 923−1473 K was verified to have a crystal structure of Zr_3O ($P6_322$) by selected area electron diffraction.

The curves of thermal expansion coefficients and Debye temperatures at finite temperatures for the three Zr_3O structures are plotted in Fig. 6. The thermal expansion coefficients plotted in Fig. 6(a) indicate that the Zr_3O ($P6_322$) has higher thermal expansion coefficient than Zr_3O ($R\bar{3}c$) and Zr_3O ($R32$) in the calculated temperature region from 0 to 1500 K. The variation of thermal expansion coefficient for the three Zr_3O structures is not so significant when the temperature is higher than 400 K since the slopes of these curves are pretty flat. Notably, the calculation result predicts a slight decrease in thermal expansion coefficient for the Zr_3O ($R\bar{3}c$) structure in the temperature range from 920 to 1500 K. During phonon vibration, the highest mode of vibration of a crystal can be presented by the Debye temperature. The value of Debye temperature reflects the interatomic bonding forces, and a higher Debye temperature means a stronger bond strength between atoms. When the temperature is close to 0 K, the differences in the Debye temperatures for these three Zr_3O structures are minimal. At the given temperatures, the highest Debye temperature was observed in Zr_3O ($R\bar{3}c$), followed by Zr_3O ($R32$) and Zr_3O ($P6_322$), as seen in Fig. 6(b). As the temperature goes from 0 to 600 K, the Debye temperature increases while reducing progressively when T>600 K, indicating that the interatomic bonding force of Zr_3O becomes stronger when the temperature rises to 600 K and then becomes weaker progressively.

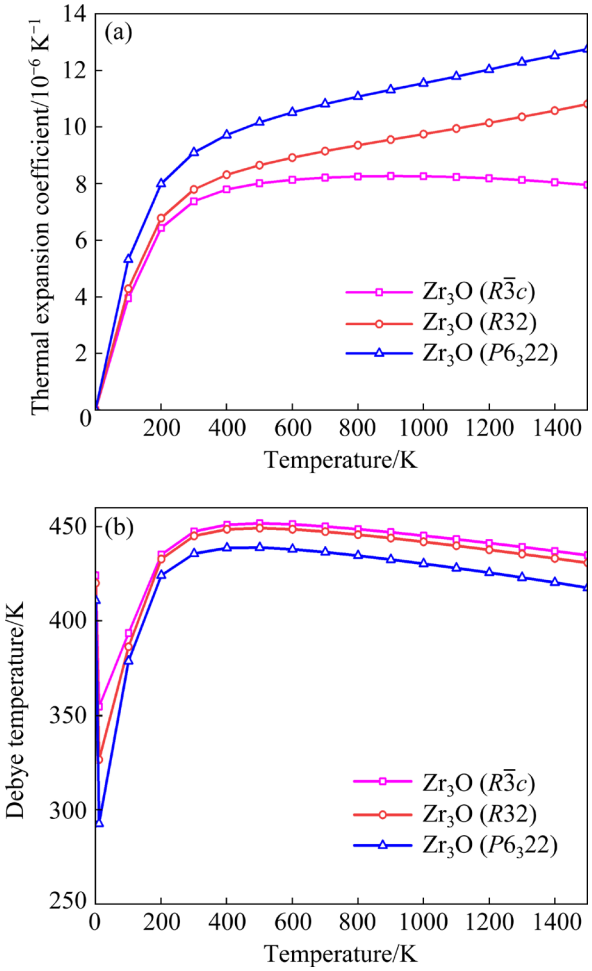

Fig. 6 Calculated thermal expansion coefficient (a) and Debye temperature (b) as function of temperature for Zr_3O ($R\bar{3}c$), Zr_3O ($R32$), and Zr_3O ($P6_322$)

The specific heat capacity at constant volume (C_V) and specific heat capacity at constant pressure (C_p) are essential thermal properties of solids. The specific heat capacities for the three Zr_3O structures under different temperatures are shown in Figs. 7(a) and (b). The values of C_V for the three Zr_3O structures are relatively close, and the values of C_p for Zr_3O ($P6_322$) are slightly higher than those of Zr_3O ($R\bar{3}c$) and Zr_3O ($R32$). From Fig. 7, both C_V and C_p show a continuous increase with increasing the temperature from 0 to 1500 K, while C_V and C_p

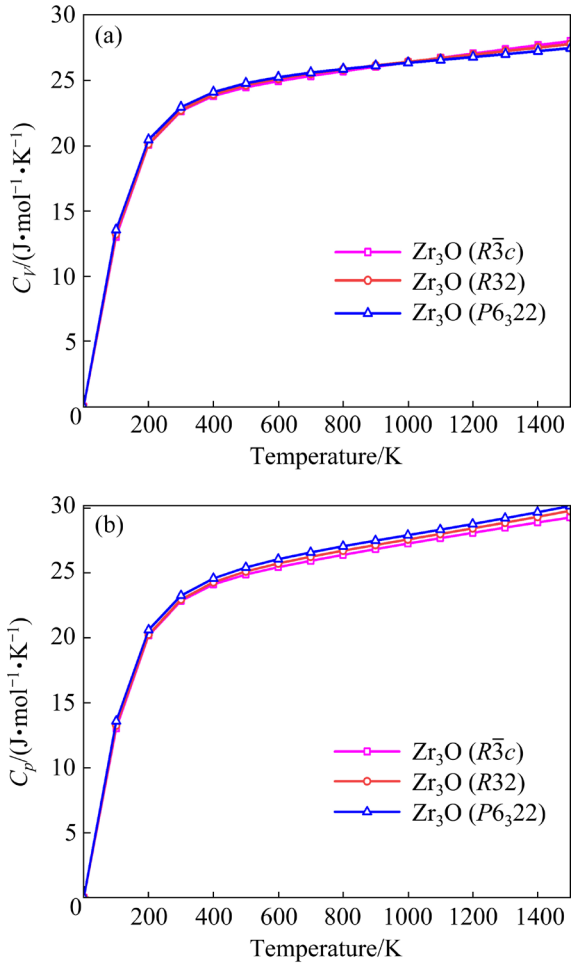

Fig. 7 Calculated specific heat capacity at constant volume (a) and pressure (b) as function of temperature for Zr_3O ($R\bar{3}c$), Zr_3O ($R32$), and Zr_3O ($P6_322$)

values of Zr_3O increase more rapidly at low temperatures. C_V approaches the Dulong−Petit limits when the temperature is higher than the Debye temperature, which is common to solids at high temperatures [45]. Therefore, it can be concluded that the effect of temperature on C_V is only in the low-temperature range ($T<\Theta$).

C_p can provide crucial insight into lattice vibrational properties. Compared with Fig. 7(a), it is evident that variations of C_p curves are similar to C_V at low temperatures. However, a distinction emerges between C_p and C_V in the high-temperature range, where C_p exhibits a continuous rise at elevated temperatures. This is because as the temperature increases to Debye temperature, the volume is constant for C_V, while the volume still expands for C_p, thus leading to continuous increase of C_p. Besides, C_p is larger than C_V for each Zr_3O, which originates from the fact that C_V has no volume expansion work while C_p does [46].

3.4 Temperature-dependent elastic properties

The temperature dependences of the isentropic elastic stiffness coefficients of the three Zr_3O structures are calculated following the approach of WANG et al [47]. The rhombohedral crystal structures have six independent elastic constants (c_{11}, c_{12}, c_{13}, c_{14}, c_{33}, and c_{44}), and the hexagonal structures have five independent elastic constants (c_{11}, c_{12}, c_{13}, c_{33}, and c_{44}), respectively. In Table 3, we list the independent elastic stiffness constants c_{ij} (GPa) of the Zr_3O ($R\bar{3}c$), Zr_3O ($R32$), and Zr_3O ($P6_322$) for some selected temperatures (0, 300, 600, 900, 1200, and 1500 K), together with the available theoretical results [14].

The present calculation results of Zr_3O ($R\bar{3}c$) are in good agreement with the calculation results from ZHANG et al [14], while different signs of c_{14} of Zr_3O ($R\bar{3}c$) are found. These discrepancies may be related to the ambiguity in the choice of the Cartesian coordinate frame for the rhombohedral structure, in which, the sign of elastic stiffness constant c_{14} in rhombohedral materials has been an open issue [48−50]. These agreements confirm the desirable accuracy of our calculations. Based on the same calculation procedure for Zr_3O ($R\bar{3}c$), we then predict the isoentropic elastic stiffness coefficients of Zr_3O ($R32$) and Zr_3O ($P6_322$). The general observation is that all the calculated c_{ij} values decrease with increasing the temperature. The large c_{33} values indicate that the suboxide Zr_3O structures are highly incompressible along the c axis.

Figure 8 presents the changes of the bulk modulus (B), shear modulus (G), Young's modulus (E), B/G ratio, and Poisson's ratio (ν) with increasing the temperature from 0 to 1500 K, respectively. With the increase in temperature, the bulk modulus, shear modulus, Young's modulus, B/G ratio, and Poisson's ratio all decrease. According to the calculated results, Zr_3O ($R32$) has the largest bulk modulus, shear modulus, and Young's modulus, while Zr_3O ($R\bar{3}c$) has the lowest. Generally, a large elastic modulus means a high hardness of materials. That is to say, Zr_3O ($R32$) is harder than the other two Zr_3O structures.

To further explore the physical properties of the three Zr_3O structures, we judge their ductility

Table 3 Independent elastic stiffness constants c_{ij} of Zr_3O ($R\bar{3}c$), Zr_3O ($R32$), and Zr_3O ($P6_322$) at different temperatures, together with available reported calculation results [14]

Phase	Space group	Temperature/K	Method	c_{ij}/GPa					
				c_{11}	c_{12}	c_{13}	c_{14}	c_{33}	c_{44}
Zr_3O	$R\bar{3}c$	0	Calc.	201	103	87	−14	214	72
			Ref. [14]	201	106	92	16	217	71
		300	Calc.	198	101	86	−13	212	71
		600	Calc.	193	99	83	−12	207	70
		900	Calc.	188	96	80	−12	203	69
		1200	Calc.	183	93	77	−11	198	68
		1500	Calc.	178	90	74	−10	194	67
Zr_3O	$R32$	0	Calc.	201	101	88	−9	221	73
		300	Calc.	199	101	87	−8	219	72
		600	Calc.	195	100	85	−8	216	71
		900	Calc.	191	98	83	−8	213	70
		1200	Calc.	187	97	82	−8	210	68
		1500	Calc.	182	95	80	−7	206	67
Zr_3O	$P6_322$	0	Calc.	199	107	86	−	229	74
		300	Calc.	196	105	84	−	226	73
		600	Calc.	192	102	81	−	222	72
		900	Calc.	187	99	77	−	217	71
		1200	Calc.	181	96	74	−	212	69
		1500	Calc.	175	92	70	−	207	67

and brittleness nature according to the Pugh's criterion [51]: B/G ratio separates ductile (>1.75) and brittle (<1.75) materials. This criterion is extended and is expected that the higher the value of B/G ratio, the more ductile the materials will be. Figure 8(d) reveals that the three Zr_3O structures are considered ductile in the temperature range from 0 to 1500 K. Among the three structures, Zr_3O ($R32$) has the largest B/G ratio, indicating that Zr_3O ($R32$) is more ductile than the other two Zr_3O structures. Additionally, the Vikers hardness (H_V) was calculated according to Ref. [52]: $H_V=2(k^2G)^{0.585}-3$, where k is the ratio of shear modulus to bulk modulus (G/B). The calculated hardness of the three Zr_3O structures falls in the range of 5−6 GPa. Notably, as reported in the literature [14,53], the bulk modulus of fully dense m-ZrO_2 is 190 GPa, the shear modulus is about 96 GPa, Young's modulus is ~250 GPa, the hardness is 10 GPa, and the B/G value is 1.97. For fully dense t-ZrO_2, the bulk modulus is around 217 GPa, the shear modulus is 99 GPa, with a Young's modulus of about 258 GPa, and a corresponding hardness value of 8.74 GPa and B/G value of 2.19 [54]. In the case of fully dense c-ZrO_2, the bulk modulus is 270.5 GPa, the shear modulus is 120 GPa, with a Young's modulus of 313.6 GPa, a hardness of 10.83 GPa, and a B/G value of 2.25 [55]. These indicate that the ductility of the suboxide Zr_3O is better than that of m-ZrO_2, but the hardness is not as good as that of m-ZrO_2, t-ZrO_2, or c-ZrO_2. Therefore, it can be concluded that forming suboxide Zr_3O during high-temperature oxidation may improve the ductility but decrease the hardness of Zr-based alloys. The above analysis contributes to a better understanding of the evolution of the mechanical properties of zirconium alloys over a wide temperature oxidation range in service.

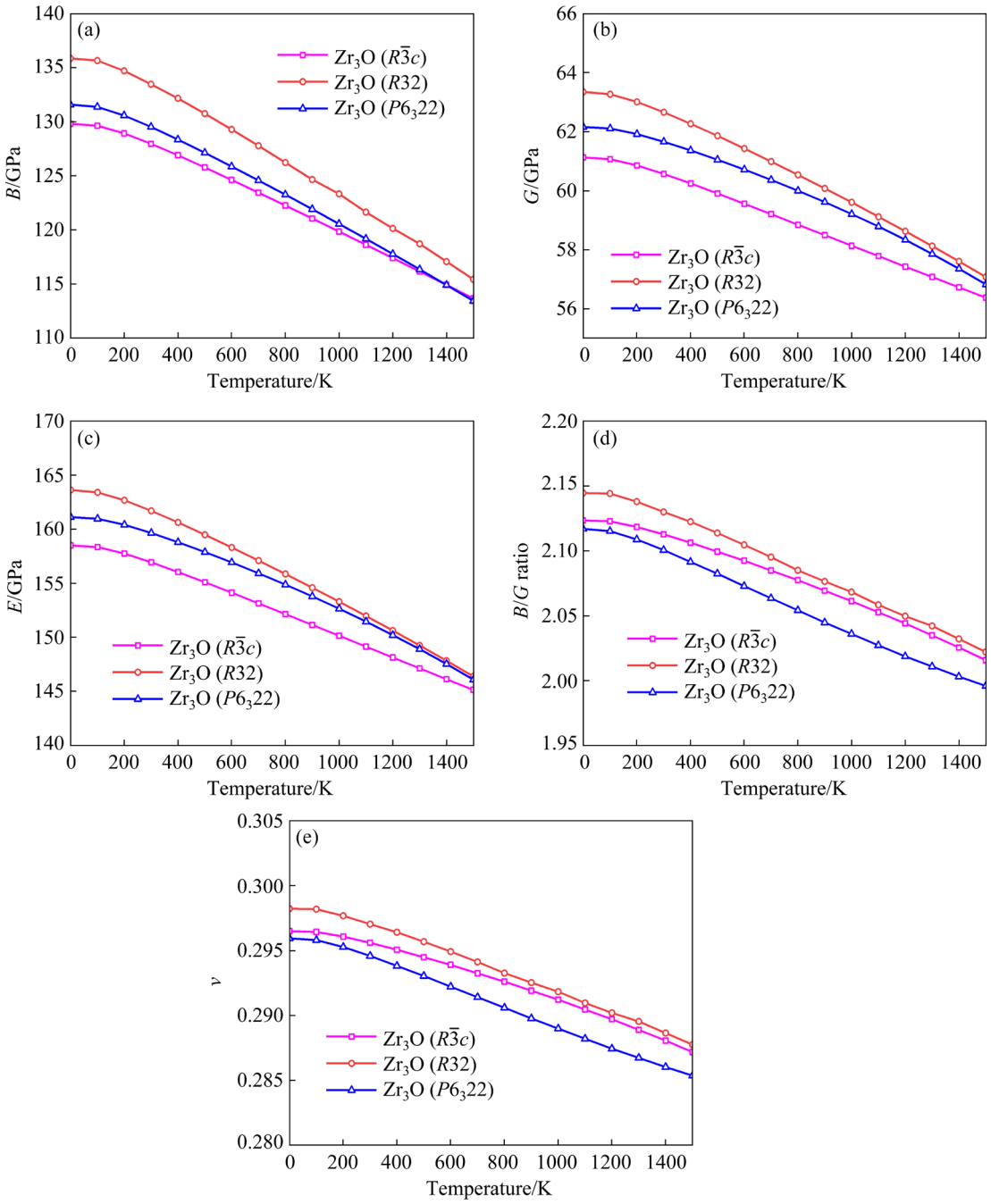

Fig. 8 Calculated bulk modulus (B) (a), shear modulus (G) (b), Young's modulus (E) (c), B/G ratio (d), and Poisson's ratio ν (e) as function of temperature for Zr_3O ($R\bar{3}c$), Zr_3O ($R32$), and Zr_3O ($P6_322$)

4 Conclusions

(1) The three Zr_3O structures are dynamically and thermodynamically stable. It is predicted that the decreasing phase stability under 0 K and 0 GPa is Zr_3O ($R\bar{3}c$) > Zr_3O ($R32$) > Zr_3O ($P6_322$), while raising temperature leads to the structural phase transitions.

(2) The phonon density of state further affirms the stability of the three Zr_3O structures. The lattice vibration of the high-frequency region of Zr_3O is attributed to the O atom, while the Zr atom determines the lattice vibration of the low-frequency region.

(3) Zr_3O ($R32$) displays superior mechanical properties compared to the other two Zr_3O phases. Results show that forming suboxide Zr_3O may improve the ductility but decrease the hardness of Zr-based alloys.

CRediT authorship contribution statement

Hong-ling ZHOU: Conceptualization, Visualization, Methodology, Data curation, Investigation, Writing − Review & editing; **Li-jun CHEN:** Conceptualization, Data curation, Writing − Review & editing; **Xiao-ling YANG:** Investigation, Methodology; **Xu-yang LIU:** Software, Resources; **Chao SUN:** Project administration, Resources, Writing − Review & editing; **Bai-feng LUAN:** Supervision, Project administration, Writing − Review & editing, Resources, Funding acquisition.

Declaration of competing interest

The authors declare that they have no known competing financial interests or personal relationships that could have appeared to influence the work reported in this paper.

Acknowledgments

This work was financially supported by the National Natural Science Foundation of China (Nos. U20A20232, U1867202). We acknowledge the National Super-computing Center in Shenzhen, China, for providing the computational resources.

References

[1] LEI Cong-yi, MAO Jian-zhong, ZHOU Dian-wu, ZHANG Xiao-min, WANG Lian. Effects of annealing treatments on forming performance of zirconium alloys [J]. Transactions of Nonferrous Metals Society of China, 2022, 32: 2908−2921.

[2] ZENG Qing-hui, CHAPUIS A, LUAN Bai-feng, LIU Qing. Slip deformation mechanism of α-Zr at 700 °C [J]. Transactions of Nonferrous Metals Society of China, 2019, 29: 1465−1475.

[3] NI Na, HUDSON D, WEI Jang-fei, WANG Peng, LOZANO-PEREZ S, SMITH G D W, SYKES J M, YARDLEY S S, MOORE K L, LYON S, COTTIS R, PREUSS M, GROVENOR C R M. How the crystallography and nanoscale chemistry of the metal/oxide interface develops during the aqueous oxidation of zirconium cladding alloys [J]. Acta Materialia, 2012, 60: 7132−7149.

[4] YANG Jian-qiao, SHANG Lun-lin, SUN Ji-yuan, BAI Shu-yuan, WANG Shu-zhong, LIU Jun-kai, YUN Di, MA Da-yan. Restraining the Cr−Zr interdiffusion of Cr-coated Zr alloys in high temperature environment: A Cr/CrN/Cr coating approach [J]. Corrosion Science, 2023, 214: 111015.

[5] CHOUDHURI G, MISHRA P, BASU S, GAYATHRI N, MUKHERJEE P, KAIN V, MUKHERJEE D, SRIVASTAVA D, DEY G K. Effect of ion and neutron irradiation on oxide of PHWR fuel tube material [J]. Journal of Nuclear Materials, 2019, 514: 12−27.

[6] KAUTZ E, GWALANI B, YU Z F, VARGA T, GEELHOOD K, DEVARAJ A, SENOR D. Investigating zirconium alloy corrosion with advanced experimental techniques: A review [J]. Journal of Nuclear Materials, 2023, 585: 154586.

[7] SONG Tian-shuo, LIU Shu-guang, CHEN Bo-han, CUI Zi-yao, ZOU Xian-rui, ZHANG Shi-liang, LI Qiang, XIA Chao-qun. Enhanced corrosion and wear resistance via thermal oxidation treatment on Zr−2.5Nb alloy for implant applications [J]. Surface and Coatings Technology, 2023, 458: 129365.

[8] NICHOLLS R J, NI N, LOZANO-PEREZ S, LONDON A, MCCOMB D W, NELLIST P D, GROVENOR C R M, PICKARD C J, YATES J R. Crystal structure of the ZrO phase at zirconium/ zirconium oxide interfaces [J]. Advanced Engineering Materials, 2015, 17: 211−215.

[9] PAN Yong, ZHANG Jin. Influence of noble metals on the electronic and optical properties of the monoclinic ZrO_2: A first-principles study [J]. Vacuum, 2021, 187: 110112.

[10] PAN Yong. Influence of oxygen vacancies on the electronic and optical properties of zirconium dioxide from first-principles calculations [J]. Journal of Electronic Materials, 2019, 48: 5154−5160.

[11] ZHAO Xu-shan, SHANG Shun-li, LIU Zi-kui, SHEN Jian-yun. Elastic properties of cubic, tetragonal and monoclinic ZrO_2 from first-principles calculations [J]. Journal of Nuclear Materials, 2011, 415: 13−17.

[12] PAN Yong. The influence of Ag and Cu on the electronic and optical properties of ZrO from first-principles calculations [J]. Materials Science in Semiconductor Processing, 2021, 135: 106084.

[13] PUCHALA B, VEN A V D. Thermodynamics of the Zr−O system from first-principles calculations [J]. Physical Review B, 2013, 88: 094108.

[14] ZHANG Jin, OGANOV A R, LI Xin-feng, DONG Hua-feng F, ZENG Qing-feng. Novel compounds in the Zr−O system, their crystal structures and mechanical properties [J]. Physical Chemistry Chemical Physics, 2015, 17: 17301−17310.

[15] ERICSSON T, ÖSTBERG G, LEHTINEN B. Some observations on Zr−O solid solutions with a microprobe and by electron microscopy [J]. Journal of Nuclear Materials, 1968, 25: 322−327.

[16] ARAI T, HIRABAYASHI M. Oxygen ordering in the Zr−O alloy: A structural, calorimetric and resistometric study [J]. Journal of the Less Common Metals, 1976, 44: 291−300.

[17] ILTIS X, MICHEL H. Transmission electron microscopy study of a locally ordered Zr−O solid solution obtained by an oxidation treatment of a Zircaloy-4 alloy [J]. Journal of Alloys and Compounds, 1991, 177: 71−82.

[18] YILMAZBAYHAN A, BREVAL E, MOTTA A T, COMSTOCK R J. Transmission electron microscopy examination of oxide layers formed on Zr alloys [J]. Journal of Nuclear Materials, 2006, 349: 265−281.

[19] SHAO Wei, LIU Can-can, WU Qiao-jun, LI Hong-tao, ANGUREL L A, FUENTE G F, JIANG Bai-ling. Comparison of in-situ oxidation behavior of Zr by micro-arc oxidation and selective laser melting [J]. Journal of the European Ceramic Society, 2022, 42: 6703−6712.

[20] WEI Tian-guo, DAI Xun, ZHAO Yi, WANG Dong, LV Jun-nan, HUANG Yun-hao, ZHANG Jun-song. ZrO phase

embedded in the oxide of Zr−Sn−Nb−Fe−Cr alloy after corrosion [J]. Journal of Nuclear Materials, 2022, 571: 153992.

[21] KŘENEK T, MIKYSEK P, POLA M, VÁLA L, MELARÉ E, JANDOVÁ V, VAVRUŇKOVÁL V, RIEGER D. Formation of metastable zirconium oxides using pulsed laser deposition of ZrO based target [C]//IOP Conference Series: Materials Science and Engineering. IOP Publishing, 2019, 613: 012016.

[22] BURTON B P, WALLE A V D, STOKES H T. First principles phase diagram calculations for the octahedral-interstitial system ZrO_X, $0 \le X \le 1/2$ [J]. Journal of the Physical Society of Japan, 2012, 81: 014004.

[23] WEI H Y, YOO C S, CHEN J Y, SHEN G Y. Oxygen-diffusion limited metal combustions in Zr, Ti, and Fe foils: Time- and angle-resolved X-ray diffraction studies [J]. Journal of Applied Physics, 2012, 111: 063528.

[24] HOLMBERG B, DAGERHAMN T. X-ray studies on solid solutions of oxygen in α-zirconium [J]. Acta Chemica Scandinavica, 1961, 15: 919−925.

[25] YAMAGUCHI S. Ordered arrangement of oxygen in the interstitial solid solution of zirconium−oxygen system [J]. Journal of the Physical Society of Japan, 1968, 24: 855−868.

[26] RIABOV A B, YARTYS V A, HAUBACK B C, GUEGAN P W, WIESINGER G, HARRIS I R. Hydrogenation behaviour, neutron diffraction studies and microstructural characterisation of boron oxide-doped Zr−V alloys [J]. Journal of Alloys and Compounds, 1999, 293/294/295: 93−100.

[27] DUBERTRET A, LEHR P. Description d'une surstructure Zr_3O_{1-x} [J]. Comptes Rendus Hebdomadaires des Séances de l'Académie des Sciences. Série C, Sciences Chimiques, 1968, 267: 820−822. (in French)

[28] DUBERTRET A, LEHR P. Description d'une surstructure Zr_3O [J]. Comptes Rendus Hebdomadaires des Séances de l'Académie des Sciences. Série C, Sciences Chimiques, 1969, 268: 501−504. (in French)

[29] WANG Y, YAN M, ZHU Q, WANG W Y, WU Y D, HUI X D, OTIS R, SHANG S L, LIU Z K, CHEN L Q. Computation of entropies and phase equilibria in refractory V−Nb−Mo−Ta−W high- entropy alloys [J]. Acta Materialia, 2018, 143: 88−101.

[30] YANG Song-ge, WANG Yi, LIU Zi-kui, ZHONG Yu. Ab initio studies on structural and thermodynamic properties of magnetic Fe [J]. Computational Materials Science, 2023, 227: 112299.

[31] YU Wei, CHONG Xiao-yu, GAN Meng-di, WEI Yan, ZHANG Ai-min, HU Chang-yi, FENG Jing. Effect of alloying elements on thermoelastic properties of Pt-based alloys [J]. Transactions of Nonferrous Metals Society of China, 2023, 33: 1851−1861.

[32] XIE Jian-jun, GIRONCOLI S D, BARONI S, SCHEFFLER M. First-principles calculation of the thermal properties of silver [J]. Physical Review B, 1999, 59: 965−969.

[33] TETER D M, GIBBS G V, BOISEN M B, ALLAN D C, TETER M P. First-principles study of several hypothetical silica framework structures [J]. Physical Review B, 1995, 52: 8064−8073.

[34] DICKINSON J M, ARMSTRONG P E. Temperature dependence of the elastic constants of molybdenum [J]. Journal of Applied Physics, 1967, 38: 602−606.

[35] DAVENPORT T, ZHOU L, TRIVISONNO J. Ultrasonic and atomic force studies of the martensitic transformation induced by temperature and uniaxial stress in NiAl alloys [J]. Physical Review B, 1999, 59: 3421−3426.

[36] ZHOU Jia-qiang, HU Biao, LI Ben-fu, DU Yong, WANG Jiong. Experimental investigation and thermodynamic modeling of Cu−Nb−Si system [J]. Transactions of Nonferrous Metals Society of China, 2023, 33: 824−838.

[37] WANG Yi, CHEN Long-qing, LIU Zi-kui. YPHON: A package for calculating phonons of polar materials [J]. Computer Physics Communications, 2014, 185: 2950−2968.

[38] ARAMBERRI H, CAZORLA C, STENGEL M, ÍÑIGUEZ J. On the possibility that $PbZrO_3$ not be antiferroelectric [J]. NPJ Computational Materials, 2021, 7: 196.

[39] PAN Yong. First-principles investigation of structural stability, electronic and optical properties of suboxide (Zr_3O) [J]. Materials Science and Engineering B, 2022, 281: 115746.

[40] BENDAOUD H, BOUHAFS B. Cubic and tetragonal phases competition of magnetic $Ru_2VZ(Si;Ge)$ Heusler compounds: Ab initio investigation [J]. Solid State Communications, 2023, 366/367: 115161.

[41] LI Meng, CORTIE L D, LIU Ji-xing, YU De-hong, ISLAM S M N, ZHAO Lan-ling, MITCHELL R G D, MOLE A R, CORTIE B M, DOU Shi-xue, WANG Xiao-lin. Ultra-high thermoelectric performance in graphene incorporated Cu_2Se: Role of mismatching phonon modes [J]. Nano Energy, 2018, 53: 993−1002.

[42] LIU Yi-zhe, ZHANG Xu-dong, BI Han-jia, LIU Xiao-qian, WANG Feng. First-principles prediction of structure, mechanical and thermodynamic properties of $Bi_xGe_yO_z$ ternary bismuth crystals [J]. Vacuum, 2022, 195: 110696.

[43] FOORD D T, NEWCOMB S B. Instabilities in the oxidation behaviour of Zircaloy-4 [C]// Proceedings of the Second International Conference on the Microscopy of Oxidation. London: The Institute of Materials, 1993: 374−386.

[44] CHEN Li-jun, LUAN Bai-feng, MA Shu-yu, WAN Peng, BAI Guang-hai, LIU Yin-li, ZHANG Yan-wei. Characteristics of the oxides and suboxides on Zr−1.0Nb−0.01Cu isothermally oxidized in steam at 650−1200 °C [J]. Corrosion Science, 2023, 210: 110825.

[45] PETIT A T, DULONG P L. Recherches sur quelques points importants de la Théorie de la Chaleur [J]. Annales de Chimie et de Physique, 1819, 14: 189−198. (in French)

[46] BAO Long-ke, KONG Zhuang-zhuang, QU De-yi, DUAN Yong-hua. The mechanical and thermodynamic properties of ZrTM (TM=Fe, Ru and Os) intermetallics under pressure and temperature: A first-principles predictions [J]. Journal of Physics and Chemistry of Solids, 2020, 142: 109465.

[47] WANG Yi, WANG Jian-jun, ZHANG Hui, MANGA V R, SHANG Shun-li, CHEN Long-qing, LIU Zi-kui. A first-principles approach to finite temperature elastic constants [J]. Journal of Physics: Condensed Matter, 2010, 22: 225404.

[48] PAGE Y L, SAXE P. Symmetry-general least-squares extraction of elastic data for strained materials from ab initio calculations of stress [J]. Physical Review B, 2002, 65: 104104.

[49] BECHMANN R. Elastic and piezoelectric constants of alpha-quartz [J]. Physical Review, 1958, 110: 1060−1061.
[50] GOLESORKHTABAR R, PAVONE P, SPITALE J, PUSCHNIG P, DRAXL C. ElaStic: A tool for calculating second-order elastic constants from first principles [J]. Computer Physics Communications, 2013, 184: 1861−1873.
[51] PUGH S F. XCII. Relations between the elastic moduli and the plastic properties of polycrystalline pure metals [J]. Philosophical Magazine, 1954, 45: 823−843.
[52] CHEN Xing-qiu, NIU Hai-yang, LI Dian-zhong, LI Yi-yi. Modeling hardness of polycrystalline materials and bulk metallic glasses [J]. Intermetallics, 2011, 19: 1275−1281.
[53] CHAN S K, FANG Y, GRIMSDITCH M, LI Z, NEVITT M V, ROBERTSON W M, ZOUBOULIS E S. Temperature dependence of the elastic moduli of monoclinic zirconia [J]. Journal of the American Ceramic Society, 1991, 74: 1742.
[54] FAN Zhou, WANG Yang, ZHANG Yi-dong, LIU Jian-yi. Influence of oxygen vacancy compensation on the structure, electronic and mechanical properties of yttrium stabilized tetragonal zirconia [J]. Materials Science in Semiconductor Processing, 2021, 135, 106082.
[55] MUHAMMAD A N, TARIQ M, ABRAR A Z, NAEEM A, TALAB H, MUHAMMAD A S, FAZAL E A, AAMIR S, JAFAR R, CHUANBAO C. Electronic, optical and elastic properties of cubic zirconia (c-ZrO_2) under pressure: A DFT study [J]. Physica B: Condensed Matter, 2021, 604: 412462.

低价锆氧化物 Zr_3O 的结构、热力学和弹性性质第一性原理研究

周虹伶[1]，陈莉君[1]，杨晓玲[1]，刘许旸[2]，孙 超[3]，栾佰峰[1,4]

1. 重庆大学 材料科学与工程学院 轻合金材料国际合作联合实验室，沈阳材料科学国家研究中心，重庆 400044；
2. 重庆大学 航空航天学院，重庆 400044；
3. 中国核动力研究设计院 反应堆燃料及材料重点实验室, 成都 610213;
4. 重庆大学 机械传动国家重点实验室，重庆 400044

摘 要：采用第一性原理系统地研究 3 种 Zr_3O 晶形 (空间群分别为 $R\bar{3}c$ (斜方六面体)、$R32$ (斜方六面体) 和 $P6_322$ (六面体))的晶格动力学及其与温度相关的热力学和力学性质。计算得到的 3 种 Zr_3O 晶形的晶体结构参数与实验结果一致。此外，证明 3 种 Zr_3O 结构在动力学和热力学上均具有稳定性。获得了 3 种 Zr_3O 晶形在 0~1500 K 温度范围内的熵、焓、吉布斯自由能、比热容、热膨胀系数和弹性模量等性质。发现 3 种 Zr_3O 晶形在 0 K 时的相对稳定性顺序为 Zr_3O ($R\bar{3}c$) > Zr_3O ($R32$) > Zr_3O ($P6_322$)；然而，在 50 K 时 Zr_3O ($R\bar{3}c$)转变成 Zr_3O ($R32$)，在 540 K 时转变为 Zr_3O ($P6_322$)。相较于其他 2 种 Zr_3O 相，Zr_3O ($R32$)表现出更优越的力学性能。

关键词：第一性原理；Zr_3O；晶格动力学；热力学性质；弹性模量

(Edited by Wei-ping CHEN)